Journal of Materials Chemistry C

ROYAL SOCIETY OF CHEMISTRY

PAPER

View Article Online
View Journal

Check for updates

Cite this: DOI: 10.1039/d5tc04500b

Enhanced functional properties of ABC-type atomic layer deposited Ru thin films for advanced Cu alternative nanoscale interconnects

Jeongha Kim,[a] Debananda Mohapatra,[ab] Yeseul Son,[a] Jae Min Jang,[c] Sang Bok Kim,[a] Tae Eun Hong,[d] Taehoon Cheon,[e] Bonggeun Shong[f] and Soo-Hyun Kim*[ab]

Atomic layer deposition (ALD) technology requires high-temperature processes to achieve low resistivity, large grain size, and fewer impurities in ultrathin interconnects; however, the thermal stability of the precursor often constrains this approach. This study presents a novel ABC-type ALD process, using [tricarbonyl(trimethylenemethane)ruthenium, [Ru(TMM)$(CO)_3$]] as the Ru precursor and two counter-reactants (O_2 and NH_3) sequentially, to deposit highly conductive ruthenium (Ru) thin films at a high temperature of 310 °C. A key innovation of this work is that grain growth occurs without the need for annealing. Compared to the conventional AB-type Ru ALD process, the ABC-type process significantly reduces resistivity from 20.1 μΩ cm to 13.4 μΩ cm. In addition to resistivity reduction, the process also improves surface roughness and reduces impurities in the Ru film. Using the Fuchs-Sondheimer and Mayadas–Shatzkes' model, the study quantitatively identifies the contribution of various factors to achieving low resistivity, highlighting grain size as the critical factor for this achievement. Moreover, machine learning potential (MLP) analysis was used to explore the adsorption and decomposition mechanisms of NH_3, providing valuable theoretical insights that support the chemical rationale behind the surface reactions. Finally, the Ru thin films deposited by the ABC-type Ru ALD process achieve excellent step coverage on high-aspect-ratio trench patterns (~30, opening width: 140 nm), presenting a breakthrough approach for next-generation nanoscale interconnects.

Received 24th December 2025,
Accepted 10th March 2026

DOI: 10.1039/d5tc04500b

rsc.li/materials-c

Open Access Article. Published on 12 March 2026. Downloaded on 4/4/2026 11:51:12 PM.
This article is licensed under a Creative Commons Attribution 3.0 Unported Licence.

1. Introduction

Scaling down semiconductor devices has enabled the fabrication of high-performance and high-speed devices while simultaneously demanding complicated three-dimensional nanostructures per Moore's law.[1,2] Since the late 1990s, copper (Cu) has been widely used as an interconnect material in semiconductor devices due to its low bulk resistivity (ρ_0: 1.7 μΩ cm) and better reliability compared to aluminum (Al).[1] However, as semiconductor devices continue to scale, metal interconnect continuously shrinks. At such diminutive dimensions, the Ta/TaN liner/barrier bilayer, which is essential for Cu interconnect, takes up a significant amount of space, significantly increasing the resistivity of the metal line.[2] Also, the scaling of semiconductor devices continues, and the width of the metal interconnect is continuously shrinking, requiring an alternate interconnect metal to Cu. As the width of the metal interconnect becomes smaller than the bulk electron mean free path (λ: 40 nm) of Cu, the resistivity increases because the electrons are scattered at the surface and grain boundaries.[2–4] Table S1 comprehensively shows the comparison of various metals being considered as potential alternatives to Cu for interconnect applications. Among these, ruthenium (Ru) has a competitive low bulk resistivity (7.1 μΩ cm), and a high work function (4.7 eV) with a shorter electron mean free path of 6.6 nm.[1,5] In addition, it has a relatively high melting temperature (2334 °C), which can improve the reliability and thermal stability of metal interconnects and is relatively less expensive than other PGMs.[6,7] For an advanced metallization process involving complex 3D structures, a precise and atomically controlled layer-by-layer uniform

[a] Graduate School of Semiconductor Materials and Devices Engineering, Ulsan National Institute of Science and Technology (UNIST), Ulju-gun, Ulsan 44919, Republic of Korea. E-mail: soohyunsq@unist.ac.kr
[b] Department of Materials Science and Engineering, Ulsan National Institute of Science and Technology (UNIST), Ulju-gun, Ulsan 44919, Republic of Korea
[c] Department of Chemical Engineering, Hongik University, Mapo-gu, Seoul, 04066, Republic of Korea
[d] Korea Basic Science Institute (KBSI) 618-230, Gangseo-gu, Busan 46742, Republic of Korea
[e] R&D Center, CTH Corporation, Daegu, 43018, Republic of Korea
[f] Advanced Materials and Semiconductor Engineering, Materials Science and Chemical Engineering, Hanyang University, Ansan-si, Gyeonggi-do 15588, Republic of Korea

Open Access Article. Published on 12 March 2026. Downloaded on 4/4/2026 11:51:12 PM.
This article is licensed under a Creative Commons Attribution 3.0 Unported Licence.

thin film formation is required, making the atomic layer deposition (ALD) industrial technique inevitable. Its ability to control thickness at the atomic layer level through self-limiting surface reactions enables uniform thin film deposition even on high aspect ratio structures.[8,9]

Low resistivity, larger grain sizes, fewer impurities, and lower surface roughness are the most critical factors affecting the semiconductor metal interconnects.[10,11] For instance, in the case of a metal ALD process, the deposition temperature increases, and the properties of the thin films, such as grain size and resistivity, typically improve which is detailed in Table S2. In a TiN ALD process using a $TiCl_4$ precursor and NH_3 reactant, the resistivity of the thin film decreases as the deposition temperature increases from 350 °C to 500 °C.[12] Similarly, in the case of a Ru ALD process using the (ethylbenzene)(1,3-cyclohexadiene)Ru(0) (EBCHDRu) precursor and O_2 reactant, the resistivity of a Ru thin film decreased from 46 000 μΩ cm to 14 μΩ cm as the deposition temperature increased from 140 °C to 310 °C, resulting in dense, well-developed polycrystalline grains and a large grain size.[11] However, when exceeding the ALD window, an optimal deposition temperature condition, the targeted precursor loses its stability, resulting in uncontrolled thermal decomposition reactions. Such decomposition can lead to unusual increases in deposition rate, uneven film growth, or the inclusion of impurities.[13–16] Taking an example of earlier reported Ru ALD process using the isopropylmethylbenzene-cyclohexadiene Ru(0) (IMBCHRu) precursor and O_2 reactant, the resistivity of Ru decreased to 30 μΩ cm as the deposition temperature increased from 185 °C to 270 °C, and again when the deposition temperature was increased to 310 °C, the resistivity increased to 40 μΩ cm. This further reduces crystallinity, increases carbon impurities, and decreases conformality at high aspect ratios occurring in the deposited Ru thin films.[17] This phenomenon is not limited to the Ru ALD process but is extended to other metal ALD processes, as shown in a comparative analysis in Table S3.

Therefore, as discussed above, a different ALD approach is imperative for the high-temperature deposition of Ru thin films. We have introduced a new Ru ALD process that sequentially introduces additional reactant gases and controls them precisely to reduce impurity concentrations and resistivity. We designate this approach as the ABC-type Ru ALD process, which is fundamentally different from the conventional AB-type Ru ALD process in terms of both the overall process and the quality of thin films. In addition, we have summarized the characteristics, advantages, and limitations of physical vapor deposition (PVD), chemical vapor deposition (CVD), ALD, and ABC-type ALD processes in Table S4. This comparison allows for a clear understanding of the strengths and limitations of each deposition method. Furthermore, it supports the superior performance of the ABC-type ALD process for Ru thin film deposition at high temperatures. For instance, a study studying the plasma-enhanced palladium (Pd) ALD process using the palladium(II)hexafluoroacetylacetonate [$Pd(hfac)_2$] precursor and various plasmas such as H_2*, NH_3*, and O_2* was carried out. When only reducing co-reactants such as H_2* or NH_3* were used, many carbon impurities were included, but adding O_2* plasma decreased the impurity concentration (17 at% → 1 at%).[18] In addition, it was reported that the resistivity of a TiN thin film deposited with only a $TiCl_4$ precursor and NH_3 reactant was 250 μΩ cm, but when zinc (Zn) was injected as an additional reactant, the resistivity decreased to 50 μΩ cm.[19] As such there have been many studies on improving the properties of thin films through an ABC-type process, including not only precious metals such as Pd, Ru, and iridium (Ir), but also nitride materials such as TiN and NbN, and oxide materials such as Al_2O_3 and HfO_2, and the contents are summarized in Table 1. An ABC-type ALD process utilizing additional reactant gases can be anticipated to produce Ru metal thin films with superior properties. By referring to various ALD process cases using these additional reactants, we aim to establish optimal process conditions to develop Ru thin films that can be stably deposited at high temperatures even when thermal decomposition of precursors occurs. This approach is crucial for advancing semiconductor interconnects, where Ru thin films with

Table 1 Summary of selected ALD processes enhancing material properties by using additional reactants

Precursor	Reactant	Additional reactant	Deposition material	Deposition temperature	Improved properties due to additional reactant	Ref.
$Pd(hfac)_2$	H_2* plasma	O_2* plasma	Pd	100 °C	Reduced impurities (C: 17 at% → 1 at%)	18
$TiCl_4$	NH_3	H_2S	TiN	400 °C	Reduced impurities (Cl: 3 ~ 7% → 1%)	20
TMA	H_2O	O_3	Al_2O_3	300 °C	Reduced impurities (C(× 10^{19} cm^{-3}): 5.5 → 3.6, H(× 10^{21} cm^{-3}): 2.8 → 1.2)	21
TDMAH	H_2O	O_3	HfO_2	275 °C	Reduced impurities (C: 7.2% → 1%, N: 4.1% → 1%) Increased GPC (0.99 Å per cyc. → 1.09 Å per cyc.)	22
$NbCl_5$	NH_3	H_2S	NbN	400 °C	Reduced impurities (Cl: 3.7 at% → 2.1 at%) Reduced resistivity (955 μΩ cm → 806 μΩ cm)	23
$TiCl_4$	NH_3	Zn	TiN	500 °C	Lower resistivity (250 μΩ cm → 50 μΩ cm)	19
WF_6	NH_3	B_2H_6	WN_x	300 °C	Lower resistivity (~ 4500 μΩ cm^{24} → 350 μΩ cm)	25
EBCHDRu	O_2	H_2	Ru	250 °C	Reduced resistivity (33 μΩ cm → 26 μΩ cm)	26
$Ir(acac)_3$	O_2	H_2	Ir	275 °C	Reduced resistivity (~11 μΩ cm → ~9.5 μΩ cm)	27
HCDS	NH_3	TBC	SiN_x	600 °C	Enhanced film conformality (88% → 105%)	28
$Ru(EtCp)_2$	O_2	H_2	Ru	150 °C	Lower deposition temperature (270 °C^{29} → 150 °C)	30

*$Pd(hfac)_2$: palladium(II)hexafluoroacetylacetonate. *TMA: trimethylaluminium. *TDMAH: tetrakis(dimethylamino)-hafnium. *EBCHDRu: ethylbenzene(1,3-butadiene)ruthenium(0). *$Ir(acac)_3$: iridium acetylacetonate. *HCDS: hexachlorodisilane. *TBC: *tert*-butyl chloride. *$Ru(EtCp)_2$: bis-(ethylcyclopentadienyl)ruthenium.

 This journal is © The Royal Society of Chemistry 2026

Open Access Article. Published on 12 March 2026. Downloaded on 4/4/2026 11:51:12 PM. This article is licensed under a Creative Commons Attribution 3.0 Unported Licence.

high-temperature sustainability properties are anticipated to play a significant role in developing next-generation devices that replace Cu interconnects.

2. Results and discussion

2.1. Selection of an optimal additional reactant for the ABC-type Ru ALD process

The thermal stability of the $Ru(TMM)(CO)_3$ precursor was verified in a traveling-wave type ALD reactor by only providing the Ru precursor into the reaction chamber without counter reactant (O_2) pulsing. No film growth was observed at 220 °C and 260 °C, while the deposition happened at 310 °C, indicating the decomposition of the precursor (Fig. S1). This suggests that the $Ru(TMM)(CO)_3$ precursor is stable up to 260 °C under typical deposition conditions and that growth is possible at 310 °C without any counter reactant pulsing due to partial thermal decomposition of the Ru precursor. Therefore, in this study, we aimed to mitigate the property degradation due to the thermal decomposition of the $Ru(TMM)(CO)_3$ precursor by introducing an ABC-type Ru ALD process using additional reactant gases and conducted experiments to compare the properties of Ru thin films deposited by the AB-type Ru ALD and ABC-type Ru ALD processes at 310 °C.

Generally, the Ru metal ALD process uses O_2 as a reactant.[31] Initially, the Ru precursor adsorbs onto the substrate surface, after which the introduction of O_2 forms an oxygen-rich surface, allowing for further precursor adsorption.[31,32] During this step, the ligands of the Ru precursor undergo reactions with surface oxygen, forming H_2O and CO_2. Subsequently, O_2 molecules dissociatively chemisorb onto the Ru surface, reacting with residual carbon species to produce CO_2 and CO gases.[31] Under these conditions, Ru films deposited using O_2 as a reactant exhibit excellent properties such as high conductivity and approximately ~100% step coverage. However, when the ALD process is conducted at a high temperature where thermal decomposition of the precursor occurs, the decomposition is expected to occur in the gas phase rather than on the substrate surface. This can result in organic residues from the precursor ligands transforming into non-volatile compounds or reacting with surface oxygen to become impurities. An increase in impurities within the film can lead to reduced grain size, thereby increasing the film's resistivity.[17] Additionally, the high temperatures from the thermal decomposition of the precursor can lead to the degradation of the film's crystallinity.[17] An ABC-type Ru ALD process was conducted to resolve these issues, which supplies additional reactive gas in a smart control.

Therefore, NH_3 or H_2, which have strong reducing properties, was selected as an additional reactant gas candidate to remove impurities such as C or O compounds that may occur during the high-temperature ALD process and to form high-quality thin films. Four experiments were conducted in total, with the precursor, main reactant, and additional reactant combinations as follows: Ru–O_2–NH_3, Ru–NH_3–O_2, Ru–O_2–H_2, and Ru–H_2–O_2. The additional reactant gases were injected at a flow rate of 50 sccm for 30 seconds, while the precursor and O_2 reactant pulse and all purge steps were each conducted for 10 seconds. All ALD processes were performed at a temperature of 310 °C for 150 cycles, using SiO_2/Si substrates. Additionally, for comparison, a standard AB-type Ru ALD process was conducted at 310 °C where precursor thermal decomposition occurs. All steps were carried out for 10 seconds each, and the process was performed for 150 cycles. The resistivity of the thin films obtained from the AB-type Ru ALD and ABC-type Ru ALD experiments with various additional reactant gases was measured (Fig. S2). The AB-type ALD exhibited relatively thicker films with a thickness of 37.3 nm, and despite the thick film, it showed a high resistivity (~18.2 μΩ cm) due to the precursor thermal decomposition. In contrast, the ABC-type ALD processes generally resulted in thinner films and lower resistivity compared to that of the AB-type process; particularly, the Ru film deposited using the Ru–O_2–NH_3 process with NH_3 as an additional reactant exhibited the lowest resistivity (~14.4 μΩ cm). In addition, XRD analysis revealed that films deposited using NH_3 exhibited significantly improved crystallinity compared to those deposited using H_2, further supporting the suitability of NH_3 as the additional reactant. Consequently, NH_3 was selected as the additional reactant gas for the ABC-type Ru ALD process.

2.2. Comparative performance of ABC-type Ru ALD processes to the conventional Ru ALD

Fig. 1(a) shows the resistivity data according to the NH_3 pulsing time, along with the resistivity data of the Ru films deposited in four steps at 220 °C and 310 °C, respectively, for comparison. This experiment was conducted to optimize the ABC-type Ru ALD process. The film thicknesses of all ABC-type Ru ALD processes were maintained at 17~18 nm. The resistivity of the ABC-type Ru films decreased as the NH_3 pulsing time increased from 10 to 30 seconds, but there was no significant change even after 30 seconds. Therefore, when the NH_3 pulsing time was set to 30 seconds, the resistivity was measured to be ~14.5 μΩ cm, and the NH_3 pulsing time for all subsequent ABC-type Ru ALD processes was fixed at 30 seconds. For comparison, the resistivity of the 25 nm Ru film deposited *via* the AB-type Ru ALD process at 220 °C and 310 °C was also measured, and the results were 17.8 μΩ cm and 20.1 μΩ cm, respectively. This confirms that the resistivity of the AB-type Ru film deposited at 310 °C (blue bar) is higher than that of the AB-type Ru film deposited at 220 °C (gray bar), which is thought to be due to partial thermal decomposition of the precursor.[17] In addition, the resistivity tends to decrease with increasing film thickness.[33] Considering the similar thickness of 17–18 nm produced by the ABC-type Ru ALD process, if the ABC-type Ru ALD film is increased to 25 nm, the resistivity of the ABC-type film is expected to be lower than that of the 25 nm film deposited *via* the AB-type Ru ALD process. The growth characteristics of Ru thin films formed by the AB-type and ABC-type ALD processes at 220 °C and 310 °C, respectively, are depicted in Fig. 1(b). At 220 °C, where no thermal decomposition of the precursor occurs, a growth per cycle (GPC) of 1.5 Å was observed

Open Access Article. Published on 12 March 2026. Downloaded on 4/4/2026 11:51:12 PM.
This article is licensed under a Creative Commons Attribution 3.0 Unported Licence.

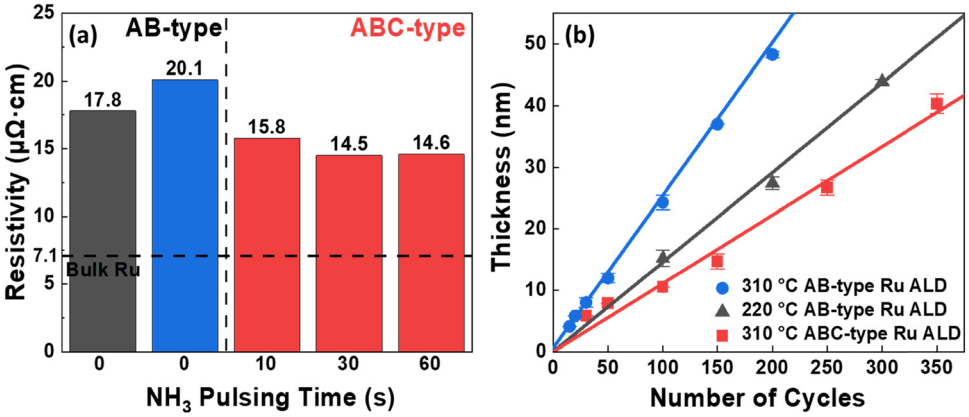

Fig. 1 ABC-type experimental process parameters optimization with additional reactants compared to the AB-type Ru ALD process. (a) The gray and blue bars represent the resistivity of approximately 25 nm thick Ru films deposited by a AB-type Ru ALD process using only $Ru(TMM)(CO)_3$ precursor and O_2 reactant without NH_3 at 220 °C and 310 °C, respectively, while the red bars show the resistivity of approximately 17–18 nm thick Ru films deposited by a ABC-type Ru ALD process with varying NH_3 exposure time at 310 °C. (b) The change in Ru film thickness is presented as a function of the number of ALD cycles for the AB-type Ru ALD process at 220 °C (gray line), and the AB-type (blue line) and ABC-type (red line) Ru ALD processes at 310 °C.

with the AB-type Ru ALD process. On the other hand, at 310 °C, the deposition temperature was higher than the decomposition temperature of the $Ru(TMM)(CO)_3$ precursor, which increased the GPC to 2.4 Å. When the precursor thermal decomposition occurs, impurities such as O and C from the ligands are injected into the thin film, increasing GPC.[17,34] Interestingly, in the ABC-type Ru ALD process using both O_2 and NH_3 as reactants, the GPC significantly decreased to 1.1 Å. In addition, no incubation cycle was observed in all three processes, and the results of the four-step process at 220 °C are consistent with previous reports.[35]

The decrease in GPC observed in the ABC-type Ru ALD process compared to the basic AB-type Ru ALD process can be attributed to the reduction in the density of oxygen atoms on the Ru surface due to the presence of NH_3. Oxygen remaining on the Ru surface plays a role in stabilizing the adsorption of Ru precursors.[31,32] However, when NH_3 is injected, it reacts with the oxygen atoms, reducing the number of chemical adsorption sites available for the Ru precursors. Therefore, a decreasing GPC phenomenon is expected, and the theoretical calculation for this will be covered later in the machine-learning potential (MLP) section. For a more precise comparison, the AB-type and ABC-type Ru ALD processes were used to produce films with a thickness of 25 nm. To achieve this thickness, the AB-type process was conducted for 100 cycles, while the ABC-type process was conducted for 250 cycles. As a result, the resistivity of the films produced by the AB-type process was 20.1 μΩ cm, whereas it decreased to 13.4 μΩ cm with the ABC-type process.

Additionally, the XRD crystallinity analysis in Fig. 2(a) reveals that the ABC-type Ru ALD process exhibits higher peak intensities across all planes, including Ru(100), Ru(002), Ru(101), Ru(102), Ru(110), Ru(103), Ru(112), and Ru(201), compared to the AB-type Ru ALD process. This indicates that using NH_3 as an additional reactant gas has improved the crystallinity of the Ru films, as evidenced by the enhanced intensity of all the major peaks of HCP-Ru. Additionally, these XRD analysis results suggest that the grain size of the Ru films has increased, which will be discussed comprehensively in the later section. Fig. 2(b) and (c) show the atomic percentages of elements as a function of sputtering depth for films deposited using the AB-type Ru ALD process and the ABC-type Ru ALD process, respectively, as determined by secondary ion mass spectrometry (SIMS) analysis. The inset graphs in Fig. 2(b) and (c) are magnified views that provide a more detailed analysis of the concentrations of impurities such as carbon (C) and oxygen (O).

As shown in the inset graphs, the concentration of C in the AB-type Ru film is 0.6 at%, and the concentration of O is 1.0 at%, resulting in a total impurity concentration of 1.6 at%. In contrast, the concentration of C in the ABC-type Ru film is less than 0.1 at%, and the concentration of O is 0.3 at%, yielding a total impurity concentration of 0.3 at%. Thus, the concentration of impurities containing C and O decreased by approximately 1.3 at% (Table S5). The ABC-type Ru thin film contains less than 0.1 at% of nitrogen (N) due to the additional reactant gas NH_3, but this amount is so small that it can be considered negligible. Matthiessen's rule was applied to explore the relationship between the reduction in impurity concentration and resistivity.

$$\rho_{total} = \rho_{bulk} + \Delta\rho_{surf} + \Delta\rho_{gb} + \Delta\rho_{impurity}$$

In the equation, the total resistivity of the metal (ρ_{total}) can be expressed as the sum of the intrinsic bulk resistivity (ρ_{bulk}), the resistivity change due to surface scattering ($\Delta\rho_{surf}$), the resistivity increase due to grain boundary scattering ($\Delta\rho_{gb}$), and the resistivity contributed by impurities ($\Delta\rho_{impurity}$).[36–38] According to previous research, it was observed that the concentration of impurities, such as C and O, was significantly low when the deposition was conducted within the ALD window temperature range (from 225 °C to 270 °C) using the

 This journal is © The Royal Society of Chemistry 2026

Open Access Article. Published on 12 March 2026. Downloaded on 4/4/2026 11:51:12 PM.
This article is licensed under a Creative Commons Attribution 3.0 Unported Licence.

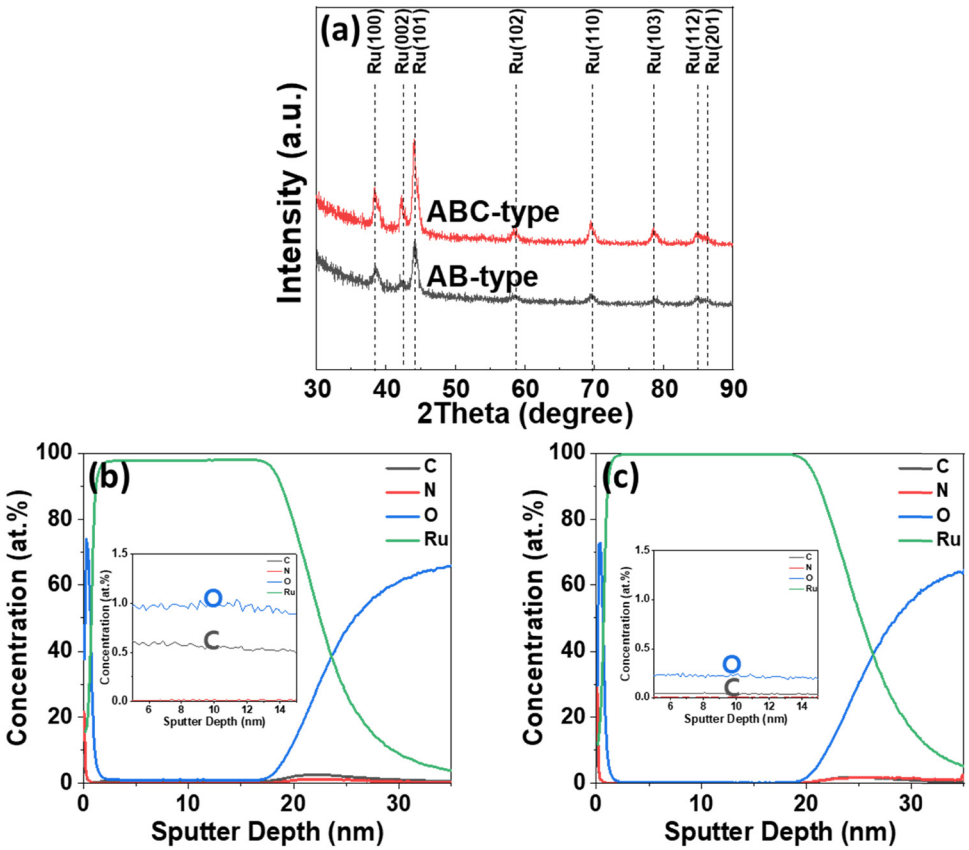

Fig. 2 (a) XRD analysis of Ru thin films with a similar thickness (approximately 25 nm) deposited on SiO_2 substrates at 310 °C after 100 ALD cycles for the AB-type process and 250 ALD cycles for the ABC-type process. (b) SIMS elemental concentration depth profiles for Ru, C, O, and N signals in the Ru/SiO_2/Si structure for the AB-type Ru ALD film and (c) the ABC-type Ru ALD film.

Ru precursor isopropyl-methylbenzene-cyclohexadiene Ru(0) (IMBCHRu) and O_2 as reactants.[17] However, it has been reported that when films are deposited at temperatures above the ALD window at 310 °C, C impurities tend to distribute uniformly within the film, increasing the film's resistivity or interfering with Ru particles' growth during deposition.[17] Thus, it can be interpreted that the reduction in C and O impurities contributed to the decrease in resistivity. However, since the concentration of impurities decreased from approximately 1.6 at% to 0.3 at% (Table S5), which is relatively small, it is necessary to investigate whether this reduction evidently influences the decrease in resistivity. A couple of reports explain the context of trace impurities' effect on the resistivity of Pt and Ru metal thin films considering their deposition temperature, GPC, grain size, *etc*, which are summarized in Table S5 for clarity.[39] It explains that the resistivity effect can be attributed to trace impurities (even minor differences in impurity levels around 0.2 at%), which either promote electron scattering or contribute to forming grain boundaries within the thin metal film.

The density and roughness of the Ru thin films were evaluated for both the AB-type and ABC-type Ru ALD processes, as the surface roughness influences the resistivity. It was analyzed through X-ray reflectometry (XRR) and densities of 11.8 g cm^{-3} and 12.3 g cm^{-3} were observed with associated roughness of 2.0 nm and 1.2 nm, respectively, for AB-type and ABC-type Ru ALD processes, highlighting the formation of a denser film with improved surface roughness for the ABC-type Ru ALD process in Fig. S3(a) and (b). Additionally, AFM analysis was performed to evaluate the surface roughness of the Ru thin films more accurately. The root mean square (R_q) roughness was found to be 1.4 nm for the AB-type Ru ALD film and 1.1 nm for the ABC-type Ru ALD film (Fig. S4). Although the AFM roughness values were slightly lower than those obtained from XRR, the trend of improved surface roughness for the ABC-type Ru film compared to the AB-type Ru film is clearly observed. In an objective to reduce the deposited Ru thin films' resistivity further, annealing was performed at 600 °C for 20 minutes in an environment of 4% H_2 and 96% Ar. The density increased to 12.1 g cm^{-3}, and the roughness was reduced to 1.0 nm, as shown in Fig. S3(c), in response to the annealed AB-type Ru thin film. In contrast, the ABC-type Ru film exhibited an improved density of 12.4 g cm^{-3} and a reduced roughness of 0.6 nm, depicted in Fig. S3(d), nearly comparable to the bulk Ru value density. The improvement in roughness for ABC-type Ru thin film can contribute to the observed reduction in resistivity and be enhanced further with an additional reactant gas supply.

According to the Mayadas and Shatzkes equation, an increase in grain size reduces the resistivity of the metal thin film.[40] The grain size of the AB-type Ru, Fig. 3(a), and ABC-type

Open Access Article. Published on 12 March 2026. Downloaded on 4/4/2026 11:51:12 PM.
This article is licensed under a Creative Commons Attribution 3.0 Unported Licence.

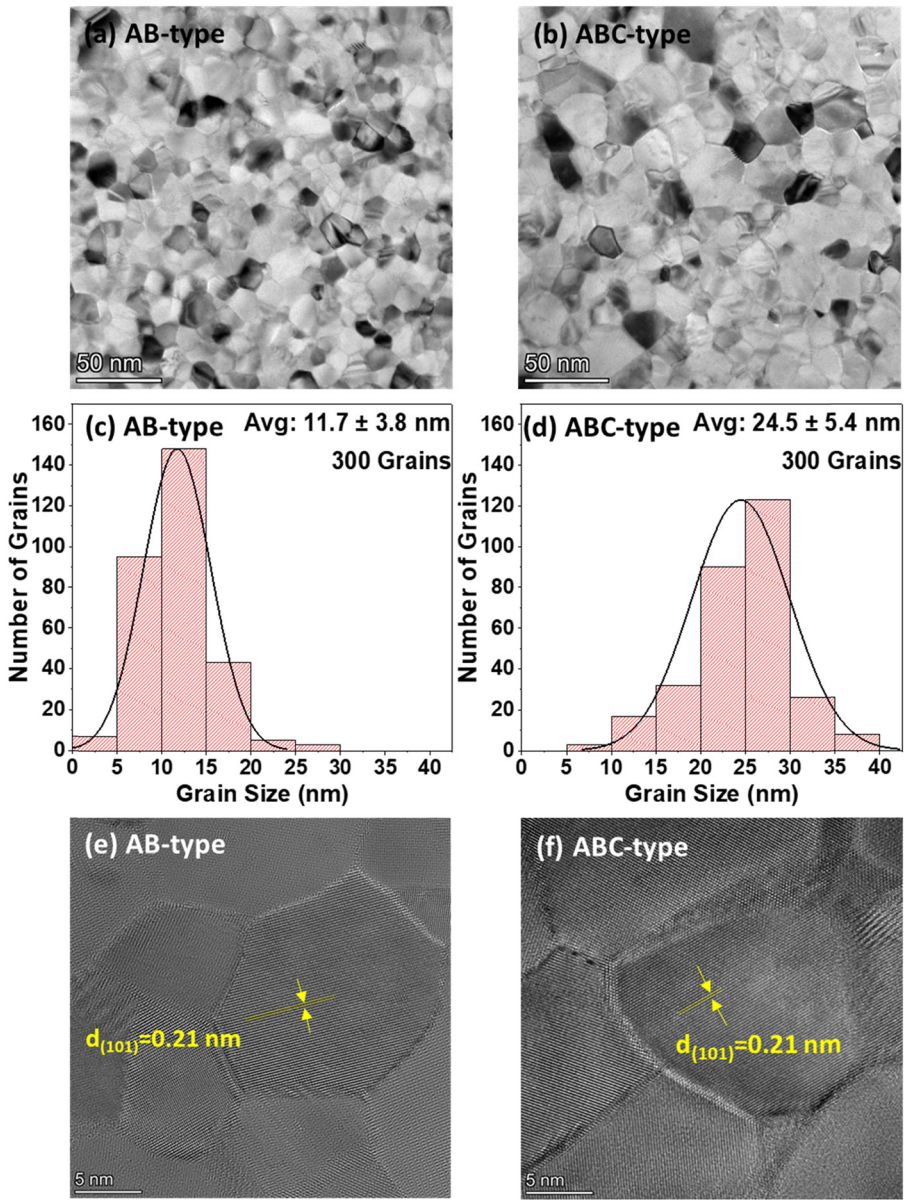

Fig. 3 Plan-view TEM bright-field (BF) images of Ru thin film deposited on a SiO_2 substrate at 310 °C with a thickness of 25 nm: (a) AB-type Ru ALD (100 ALD cycles), (b) ABC-type Ru ALD (250 ALD cycles). Average grain size distributions obtained from plan-view TEM BF images: (c) AB-type Ru ALD, (d) ABC-type Ru ALD. The grain sizes are averaged over 300 measurements. High-resolution (HR) TEM images of the Ru films: (e) AB-type Ru ALD (100 ALD cycles) and (f) ABC-type Ru ALD (250 ALD cycles).

Ru, Fig. 3(b), thin films was analyzed using plan-view bright-field (BF) TEM images to understand the material properties associated with grain growth improvement deposited on a SiO_2 substrate at 310 °C. Based on the size analysis of many grains shown in the plan-view TEM image, it was determined that the average grain size for the AB-type Ru thin film was 11.7 nm, and for the ABC-type Ru thin film, it was 24.5 nm. These average grain sizes were determined from the analysis of 300 grains as shown in the grain size distribution statistics in Fig. 3(c) and (d), respectively, indicating 12.8 nm grain growth for the ABC-type Ru thin film. This grain size analysis confirms that the injection of the additional reactant gas NH_3 facilitates grain growth, which consequently enhances the properties of the Ru metal films. Fig. 3(e) and (f) depict the high-resolution (HR-TEM) images of Ru thin films deposited through the AB-type Ru ALD and ABC-type Ru ALD processes, respectively. These results demonstrate the polycrystalline structure of the Ru films, allowing the Ru(101) plane with an interplanar spacing of approximately 0.21 nm to be observed. Fig. S5(a) and (b) show plan-view TEM dark field (DF) images of the Ru films deposited using the AB-type and ABC-type Ru ALD processes, respectively. These images also clearly confirm the polycrystalline structure of the Ru films and enlarged grain size for ABC-type Ru ALD as compared with those of the AB-type one.

Moreover, reducing impurities and increasing grain size in ALD thin films are critical for enhancing electrical performance

 This journal is © The Royal Society of Chemistry 2026

Open Access Article. Published on 12 March 2026. Downloaded on 4/4/2026 11:51:12 PM. This article is licensed under a Creative Commons Attribution 3.0 Unported Licence.

and crystallinity. As summarized in Table S6, various studies on metals show a clear trend: as the concentration of impurities decreases and the grain size increases, the resistivity of the thin films also decreases. Multiple approaches have been employed in ALD processes to minimize impurities, and it has been observed that lower impurity concentrations correspond to an increase in grain size. As the grain grows, the electron transport paths improve, reducing electron scattering and, consequently, lowering the resistivity of the films. This trend is consistently observed across metals and precursors in ALD processes, with higher deposition temperatures further accentuating these effects.[39,41]

An increase in nucleation density leads to numerous nuclei with varying orientations at multiple sites, developing many small grains. This decreases surface roughness, and consequently, the grain size of the thin film generally decreases.[42–45] However, in certain situations, an increase in grain size may still result in a decrease in roughness. In practice, surface roughness may vary due to factors such as the material composition of the thin film, deposition method, type of substrate, and deposition temperature. The observed phenomenon, where the grain size of the ABC-type Ru thin film was more prominent and the roughness improved compared to the AB-type Ru thin film, matched the previous report on similar experimental situations.[46]

To verify the conformal deposition of the high-temperature Ru ALD process with NH_3 on high aspect ratio 3D structures, deposition was conducted on a trench-patterned wafer with an aspect ratio of approximately 30 and an opening width of 140 nm. The results confirmed a step coverage of nearly 100%, with Ru deposited uniformly across the trench-patterned structures' top, middle, and bottom regions, as shown in Fig. 4(a). Additionally, further characterization of the structure was performed using energy-dispersive X-ray spectroscopy (EDS), Fig. 4(b), and high-angle annular dark field scanning transmission electron microscopy (HAADF-STEM), Fig. 4(c). The EDS mapping results shown in Fig. 4(b) demonstrate that Ru atoms are uniformly deposited across the SiO_2/Si patterned wafer. In addition, HAADF-STEM, which highlights heavier atoms with brighter contrast, confirms the deposition of Ru on the patterned wafer, as Ru, being the heaviest atom among Si, SiO_2, and Ru, appears brightest in the images. Therefore, it can be confirmed that the high-temperature ABC-type Ru ALD process provides excellent step coverage, consistent with ALD characteristics of ensuring uniform and conformal deposition.

However, it is generally observed that the step coverage tends to decrease at temperatures where precursor decomposition occurs, particularly as the aspect ratio increases.[17] In the Ru ALD process using the IMBCHRu precursor and O_2 reactant, excellent step coverage was achieved for structures with small aspect ratios, regardless of deposition temperature. However, step coverage was decreased at high temperatures exceeding the ALD window for structures with high aspect ratios. Previous studies attributed this phenomenon to a rapid increase in growth rate due to partial precursor decomposition at high temperatures, leading to uncontrolled decomposition and making uniform coating difficult.[17] However, in this study, nearly 100% conformal deposition was observed even on high aspect ratio structures at a thermal decomposition temperature of 310 °C. It is essential to consider whether the precursor decomposes in the gas phase or on the surface. As reported in a previous study, if decomposition occurs in the gas phase, there is a high possibility of non-uniform deposition on trench-structured substrates.[17] In this case, it will likely exhibit growth behavior similar to CVD rather than ALD.[47] However, it is believed that a conformal deposition, as shown in Fig. 4, is likely to occur even though the $Ru(TMM)(CO)_3$ precursor undergoes partial thermal decomposition the moment it is physically or chemically adsorbed onto the substrate surface, like the ALD process.

Possible surface reactions of NH_3 during Ru ALD were investigated using MLP calculations, as summarized in Fig. S6. From the literature, NH_3 can dissociatively adsorb on the Ru surface and exist as H and NH_x ($x = 3, 2, 1$) adsorbates.[48,49] The mechanism for such dissociative adsorption of NH_3 is shown in Fig. S6(a). Current MLP-calculated energy values for adsorption, reaction, and activation are all in good agreement with the previously reported ones obtained using DFT calculations.[49] Dissociation of NH_3 is exothermic, involving an

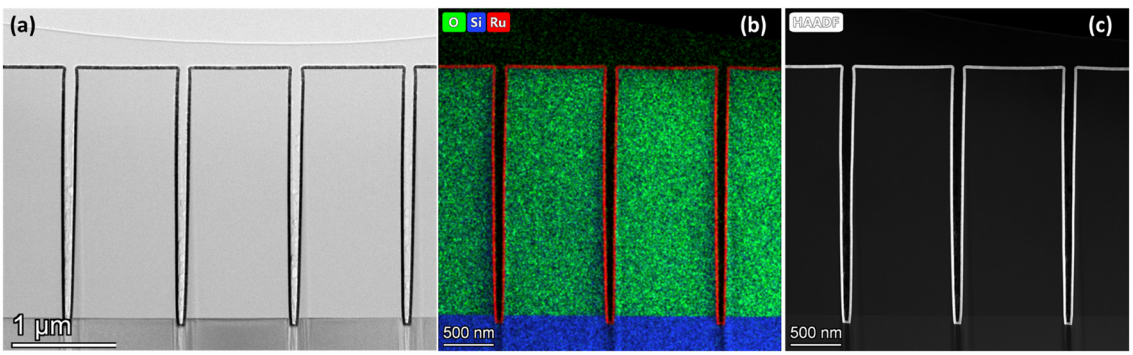

Fig. 4 Conformal deposition of high-temperature ABC-type Ru ALD process using NH_3 on high aspect ratio trench patterned substrates, resulting ~20 nm thick Ru film at 310 °C (200 ALD cycles). (a) TEM image showing ~100% step coverage of Ru on a patterned wafer with an aspect ratio of ~30 and an opening width of 140 nm. (b) EDS mapping of Ru distribution on the patterned wafer, demonstrating uniform Ru atom distribution. (c) The HAADF-STEM image highlights Ru deposition, with heavier atoms appearing brighter.

Open Access Article. Published on 12 March 2026. Downloaded on 4/4/2026 11:51:12 PM.
This article is licensed under a Creative Commons Attribution 3.0 Unported Licence.

activation energy of 1.17 eV for the initial rate-determining step. Furthermore, the diffusion barrier of atomic H on the Ru surface is calculated to be only 0.11 eV,[50,51] allowing facile surface diffusion of H. Thus, it can be expected that atomic H on the Ru surface can be supplied under exposure to NH_3 gas. Such atomic hydrogen can be expected to reduce the Ru surface, removing the oxygen originating from the O_2 pulse. For example, it is observed that the combination of atomic H and O into easily removable H_2O would be facile on the Ru surface, as shown in Fig. S6(b). The activation energy for the O–H bond formation is 1.25 eV,[52] which corresponds to a rate constant of $k = 2 \times 10^2\ s^{-1}$ at 310 °C, assuming Arrhenius kinetics with a typical pre-exponential factor of *ca.* $10^{13}\ s^{-1}$.[53] Furthermore, it is also known that the Ru surface can catalyze various reactions involving hydrocarbons,[54,55] so that the carbonaceous impurities can also be removed *via* reactions with H. As a result, it can

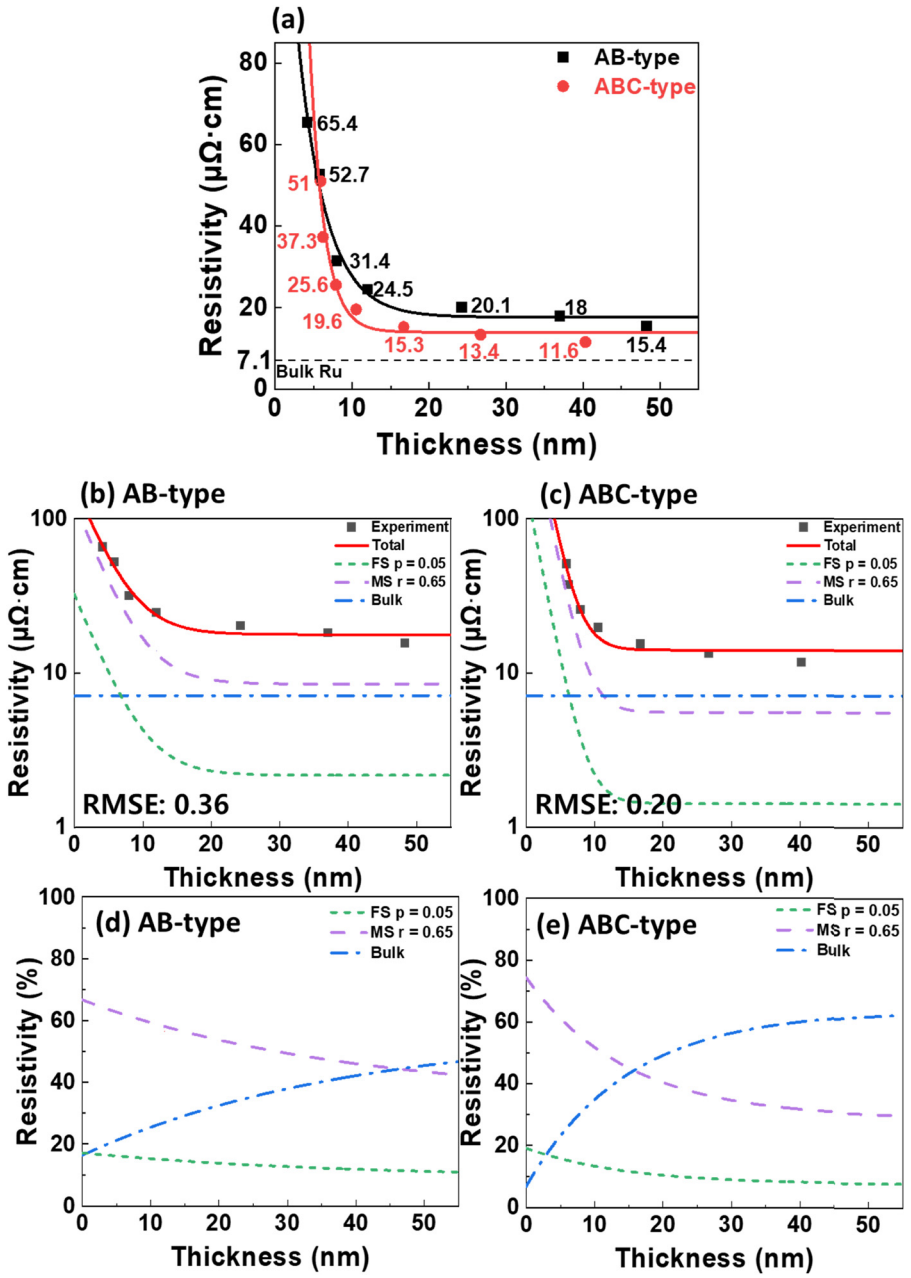

Fig. 5 The resistivity of Ru films as a function of film thickness, comparing the results of two Ru ALD processes: AB-type Ru ALD (black curve) and ABC-type Ru ALD (red curve), both conducted at 310 °C. FS-MS model-based resistivity evolution on thin film thickness deposited *via* the AB-type and ABC-type Ru ALD processes. (b) and (c) show the total resistivity of Ru films deposited *via* the AB-type and ABC-type Ru ALD processes. The measured resistivity was based on various factors, such as surface scattering (green), grain boundary scattering (purple), and bulk resistivity (blue), according to the FS–MS model. (d) and (e) illustrating the relative contributions of the factors responsible for the resistivity increase in Ru films deposited *via* the AB-type and ABC-type ALD processes.

This journal is © The Royal Society of Chemistry 2026

Open Access Article. Published on 12 March 2026. Downloaded on 4/4/2026 11:51:12 PM. This article is licensed under a Creative Commons Attribution 3.0 Unported Licence.

be understood that the impurity content of O and C on the Ru surface is reduced due to H formed during the pulse of NH_3. On the other hand, it was suggested that the oxidation of the precursor molecules by the partially oxidized surface after exposure to O_2 would result in increased GPC in the previous O_2-based study on Ru ALD.[35] Thus, the removal of such surface O by NH_3 would decrease GPC as observed in the case of the ABC-type Ru ALD process.

2.3. Comparative performance of size effects on the resistivities of ABC-type and AB-type Ru ALD thin films

According to the international roadmap for devices and systems (IRDS) technology roadmap, the minimum metal interconnect pitch in advanced microelectronic chips currently used in the industry is around 25 nm, which is expected to decrease further.[4] Therefore, comparing the resistivity reduction effects at sizes below 25 nm is necessary to match the IRDS standard. As shown in Fig. 5(a), the ABC-type Ru ALD process exhibits lower resistivity than the AB-type Ru ALD process down to a thickness of approximately 6 nm. However, for Ru films thinner than 6 nm, the film thickness becomes smaller than the electron mean free path of Ru, which is 6.6 nm, leading to an increased probability of electron scattering at the grain boundaries, causing a sharp rise in resistivity for both processes. To identify the leading causes of resistivity reduction in Ru films deposited *via* the AB-type and ABC-type Ru ALD processes, we applied the Fuchs-Sondheimer (FS) and Mayadas–Shatzkes (MS) models. Using these models, we can predict the contribution of surface scattering specularity (p) and grain boundary reflection (r) to the resistivity.[3,56,57]

$$\rho = \rho_0 + \rho_0\lambda\frac{3(1-p)}{4d} + \rho_0\lambda\frac{3r}{2D(1-r)}$$

In the above equation, bulk resistivity (ρ_0), the bulk electron mean free path (λ), film thickness (d), and grain size (D) are represented.

According to the FS model, the parameter p is a measure of whether electrons undergo diffuse scattering ($p = 0$) or specular scattering ($p = 1$) when they collide with the surface. In the case of diffuse scattering, electrons move randomly, leading to an increase in resistivity, whereas in specular scattering, the parallel momentum component of the electrons is preserved, preventing any increase in resistivity.[3] In the MS model, the parameter r represents the probability of electron reflection due to grain boundary scattering, where $r = 1$ means that all electrons are reflected at the grain boundary.[38,56,58] Fig. 5(b) and (c) illustrate the total resistivity *versus* thickness data for the AB-type and ABC-type Ru ALD processes. The root mean square error (RMSE) was 0.36 for the AB-type Ru ALD process and 0.20 for the ABC-type Ru ALD process. This indicates that the total resistivity *versus* thickness curves were fitted by varying r and p to achieve the smallest RMSE. The fitting results indicated the slightest error when the p was 0.05, and the r was 0.65. Fig. 5(d) and (e) show the relative contributions of various factors to the increase in resistivity. Based on the analysis, it was anticipated that grain boundary scattering would significantly contribute to the increase in resistivity. As expected, the graphs in Fig. 5(d) and (e) reveal that grain boundaries significantly influence resistivity, while the impact of surface scattering on its increase is relatively minor. This is consistent for both the AB-type Ru ALD and ABC-type Ru ALD processes, with the influence of grain boundary scattering becoming more pronounced as the film thickness decreases. This highlights the importance of microstructure optimization in fabricating ultrathin Ru films with low resistivity, especially at thicknesses below 10 nm. Mainly, for the ABC-type Ru ALD process, it was found that the contribution of theoretical bulk resistivity becomes dominant at Ru film thicknesses greater than approximately 15 nm while for the AB-type one, it becomes dominant from much thicker thickness, $\sim$45 nm. This is again due to the enlarged grain size of the ABC-type ALD Ru compared with the AB-type one.

3. Conclusions

Ru thin films were successfully deposited using a novel ABC-type Ru ALD process involving the addition and purging of NH_3 as an additional reactant at 310 °C. The resulting Ru films exhibited significantly improved characteristics compared to the conventional AB-type Ru ALD process. Specifically, the roughness improved from 2.0 nm to 1.2 nm, and the film density increased from 11.8 g cm^{-3} to 12.3 g cm^{-3}, indicating the formation of a denser film. MLP theoretical calculations revealed that NH_3 dissociatively adsorbed on the Ru surface, existing as H and NH_x adsorbates, which contributed to a significant reduction in impurity content, decreasing C and O from 1.6 at% to 0.3 at%. The growth rate was reduced from 2.4 Å per cycle for the AB-type Ru ALD process to 1.1 Å per cycle for the ABC-type process, which was attributed to the removal of surface oxygen by NH_3. Moreover, the average grain size increased from 11.7 nm to 24.5 nm in the ABC-type Ru ALD process, resulting in a reduction in resistivity from 20.1 μΩ cm to 13.4 μΩ cm. FS-MS model analysis quantitatively assessed the contribution of various factors to the resistivity, revealing that the grain size had the most dominant impact on the resistivity reduction. The ABC-type Ru ALD process also achieved excellent conformality, with nearly 100% step coverage on high-aspect-ratio structures. Overall, the ABC-type Ru ALD process enables the production of high-quality Ru thin films with low resistivity and large grain sizes at higher deposition temperatures, presenting a promising alternative to Cu interconnects for future semiconductor applications.

4. Experimental section

4.1. ABC-type and AB-type Ru ALD processes

Both ABC-type and AB-type Ru ALD processes were performed using a traveling wave-type thermal ALD reactor (Lucida-D200, NCD Technology, Korea). All lines in the Ru ALD experiments were fixed at a high temperature of 100 °C to prevent the

Open Access Article. Published on 12 March 2026. Downloaded on 4/4/2026 11:51:12 PM.
This article is licensed under a Creative Commons Attribution 3.0 Unported Licence.

condensation of the precursors during the delivery into the chamber. For Ru ALD, the deposition temperature was at 310 °C. All Ru thin films were deposited on 2 cm × 2 cm substrates cut from 6-inch p-type Si wafers with 100 nm thick thermally grown SiO_2. In all ALD processes for Ru, the precursor used was tricarbonyl(trimethylenemethane)ruthenium [Ru(TMM)$(CO)_3$], provided by Tanaka Precious Metals, Japan, which is a metal–organic precursor with a vapor pressure of 0.4 Torr at 10 °C, which exists as a liquid at room temperature. Therefore, this precursor was vaporized in a bubbler cooled to 10 °C and delivered to the reaction chamber using N_2 gas at a flow rate of 50 standard cubic centimeters per minute (sccm). First, the thermal stability of the Ru precursor was confirmed in the traveling wave-type thermal ALD equipment. To proceed with this, the Ru precursor was injected into the chamber at 310 °C for 20 minutes using 50 sccm of N_2 carrier gas and no reactant O_2 gas. The basic AB-type Ru ALD used Ru(TMM)$(CO)_3$ and O_2 reactants. The reactant O_2 was injected at 50 sccm. The AB-type Ru ALD experiment consisted of the following sequence: Ru(TMM)$(CO)_3$ precursor pulse - Ru(TMM)$(CO)_3$ precursor purge - O_2 reactant pulse - O_2 reactant purge. The Ru ALD timing sequences for the AB-type process were 10–10–10–10 seconds. In contrast, the ABC-type Ru ALD process consists of ABC-type: Ru(TMM)$(CO)_3$ precursor pulse - Ru(TMM)$(CO)_3$ precursor purge - O_2 reactant pulse - O_2 reactant purge - additional reactant pulse - additional reactant purge, as shown in Fig. S7. NH_3 or H_2 was used as an additional reactant gas and injected for 30 seconds. O_2, NH_3, and H_2 reactants were injected at 50 sccm. Additionally, 100 sccm of N_2 was used for 10 seconds after each injection of precursor and reactant in both AB-type and ABC-type ALD processes to remove reaction byproducts and excess untreated chemicals from the ALD reaction chamber. The Ru films were grown using the AB-type and ABC-type ALD processes at 310 °C were subjected to rapid thermal annealing (RTA, MILA-5050Z, ADVANCE RIKO, Japan) for 20 minutes in a gas mixture of 4% H_2 and 96% Ar at 20 sccm, with annealing temperatures reaching 600 °C.

4.2. Machine-learning potential (MLP) calculations

Theoretical calculations to elucidate the surface reactions were performed using the Matlantis software package, which employs a universal machine-learning potential (MLP) named PreFerred Potential (PFP) covering 96 elements.[59,60] The PFP dataset was pre-trained from density functional theory (DFT) calculations using VASP with the PBE functional. Dispersion corrections were calculated using an implementation of the D3BJ *via* the torch-dftd package.[61] Geometry optimizations were performed with a force convergence threshold of 0.001 eV Å^{-1}. The transition states were calculated using the nudged elastic band (NEB) method with a threshold of 0.05 eV Å^{-1} for the maximum force over all atoms, utilizing 17 images per calculation. The accuracy of PFP MLP toward surface chemistry of metals was benchmarked in recent studies, showing good correspondence with DFT calculations.[62,63]

$$E_{step} = E_{total} - (E_{slab} + E_{adsorbate})$$

where E_{total}, E_{slab}, and $E_{adsorbate}$ represent the structural energy of the surface with adsorbate, the energy of the surface without adsorbate, and the gas phase energy of the adsorbate molecule, respectively.

4.3. Advanced Ru ALD thin film measurements and characterization tools

Various analytical tools were used to analyze the characteristics of the AB-type and ABC-type Ru ALD processes. The thicknesses of the deposited Ru thin films were measured using a scanning electron microscope (SEM, SU8220 Cold FE-SEM, Hitachi High-Technologies, Japan) and X-ray reflectivity (XRR; D8 DISCOVERY, Bruker, USA). The phase and crystallinity of the films were analyzed using grazing incidence angle X-ray diffraction (GIAXRD; D8 DISCOVERY, Bruker, USA) with Cu K-alpha radiation (wavelength = 1.5406 Å) and an incidence angle of 0.3°. The density was determined using X-ray reflectivity (XRR; D8 DISCOVERY, Bruker, USA). The roughness of the Ru films was analyzed using X-ray reflectivity (XRR; D8 DISCOVERY, Bruker, USA) and atomic force microscopy (AFM; Multimode V, Veeco, USA). The sheet resistance of the films was measured using a four-point probe (CMT-100A, AIT, Korea), with measurements taken at a minimum of five different points on the wafer, resulting in primarily similar values. The elemental composition and purity analysis were conducted using secondary ion mass spectrometry (SIMS; IMS-7f, CAMECA, France). In the SIMS analysis, a Cs^+ gun was used with an impact energy set at 5 keV and a current of 1 nA. The detailed procedure for SIMS quantification associated with Rutherford backscattering spectrometry (RBS) data interpretations has been provided in the SI. The grain size of the films was confirmed through ultra-high resolution transmission electron microscope (UHR-TEM; Themis Z, Thermo Fisher Scientific, USA) plan-view analysis. Additionally, studies such as diffraction patterns and dark fields were all conducted using the same equipment. The step coverage of the film was evaluated by depositing the film on a trench structure with an aspect ratio of ~30 (top widths of 140 nm and bottom widths of 70 nm) and analyzing it by cross-sectional view TEM.

Conflicts of interest

There are no conflicts of interest to declare.

Data availability

The data that support the findings of this study are available from the corresponding author upon reasonable request.

Additionally, supporting data are provided as part of the supplementary information (SI). Supplementary information is available. See DOI: https://doi.org/10.1039/d5tc04500b.

Acknowledgements

This work was supported by the Nano Material Technology Development Program (Grant No. RS-2024-00408180) through the National Research Foundation (NRF) of Korea, funded by

 This journal is © The Royal Society of Chemistry 2026

Open Access Article. Published on 12 March 2026. Downloaded on 4/4/2026 11:51:12 PM. This article is licensed under a Creative Commons Attribution 3.0 Unported Licence.

the Ministry of Science, ICT, and Future Planning. This work was also supported by the Technology Innovation Program (Public-private joint investment semiconductor R&D program (K-CHIPS) to foster high-quality human resources) (RS-2023-00236667, High-performance Ru-TiN interconnects *via* high-temperature atomic layer deposition (ALD) and development on new interconnect materials based on ALD and RS-2023-00232222, High-temperature atomic layer deposition precursors and processes for dielectrics in 3D V-NAND devices) funded by the Ministry of Trade, Industry & Energy (MOTIE, Korea) (1415187401 and 1415187363).

References

1 D. Gall, *J. Appl. Phys.*, 2016, 119.
2 D. Gall, J. J. Cha, Z. Chen, H.-J. Han, C. Hinkle, J. A. Robinson, R. Sundararaman and R. Torsi, *MRS Bull.*, 2021, **46**, 959.
3 D. Gall, *J. Appl. Phys.*, 2020, 127.
4 A. A. Vyas, A. Kumar, B.-Y. Nguyen, C. K. P. Cheung, C.-P. Chang, C. Henderson, G. Klimeck, G. Bouhe, H. Bu, J. Stathis, J. Fonseca, J. Brewer, J. Barnett, L. Liebmann, M. Kodera, M. Passlack, M. Salmani, M. Badaroglu, P. Wong, P. Sarangapani, R. Liu, S. Kim, S. Mehrotra, S. Drizlikh, S. Kim, T. Nogami, W. Tsai, W. Maszara, Y. Xu and Y. Fukuzaki, IEEE, the international roadmap for devices and systems: 2023, 2023.
5 Y. Kim, M. Kim, Y. Kotsugi, T. Cheon, D. Mohapatra, Y. Jang, J. Bae, T. E. Hong, R. Ramesh, K. An and S. Kim, *Adv. Funct. Mater.*, 2022, 32.
6 A. K. Sahu, D. K. Dash, K. Mishra, S. P. Mishra, R. Yadav and P. Kashyap, in *InTech eBooks*, 2018.
7 A. Cowley, *Johnson Matthey Technol. Rev.*, 2023, **67**, 361.
8 H. C. M. Knoops, S. E. Potts, A. A. Bol and W. M. M. Kessels, *Elsevier eBooks*, 2014, pp. 1101–1134.
9 M. Leskelä and M. Ritala, *Thin Solid Films*, 2002, **409**, 138.
10 S.-H. Kim, N. Kwak, J. Kim and H. Sohn, *J. Electrochem. Soc.*, 2006, **153**, G887.
11 S. Yeo, S.-H. Choi, J.-Y. Park, S.-H. Kim, T. Cheon, B.-Y. Lim and S. Kim, *Thin Solid Films*, 2013, **546**, 2.
12 N. W. Zhang, N. J. Cai, N. D. Wang, N. Q. Wang and N. S. Wang, *IEEE*, 2010, 7.
13 H. Kim, *J. Vac. Sci. Technol., B*, 2003, **21**, 2231.
14 S. M. George, *Chem. Rev.*, 2009, **110**, 111.
15 J. Pilz, A. Perrotta, G. Leising and A. M. Coclite, *Phys. Status Solidi A*, 2019, 217.
16 S. Jeon and S. Park, *J. Electrochem. Soc.*, 2010, **157**, H930.
17 S.-H. Choi, T. Cheon, S.-H. Kim, D.-H. Kang, G.-S. Park and S. Kim, *J. Electrochem. Soc.*, 2011, **158**, D351.
18 J.-Y. Feng, M. M. Minjauw, R. K. Ramachandran, M. Van Daele, H. Poelman, T. Sajavaara, J. Dendooven and C. Detavernier, *Phys. Chem. Chem. Phys.*, 2020, **22**, 9124.
19 M. Ritala, M. Leskelä, E. Rauhala and P. Haussalo, *J. Electrochem. Soc.*, 1995, **142**, 2731.
20 H. J. Lee, J. H. Hwang, J.-Y. Park and S. W. Lee, *ACS Appl. Electron. Mater.*, 2021, **3**, 999.
21 T. Kubo, J. J. Freedsman, Y. Iwata and T. Egawa, *Semicond. Sci. Technol.*, 2014, **29**, 045004.
22 B. G. Ko, C. T. Nguyen, B. Gu, M. R. Khan, K. Park, H. Oh, J. Park, B. Shong and H.-B.-R. Lee, *Dalton Trans.*, 2021, **50**, 17935.
23 H. J. Lee, S. Y. Jang, H. M. Lee, J. Y. Sung, S. E. Kim, J. D. Jeon, Y. Yun and S. W. Lee, *J. Alloys Compd.*, 2023, **952**, 170033.
24 J. W. Klaus, S. J. Ferro and S. M. George, *J. Electrochem. Soc.*, 2000, **147**, 1175.
25 S.-H. Kim, J.-K. Kim, N. Kwak, H. Sohn, J. Kim, S.-H. Jung, M.-R. Hong, S. H. Lee and J. Collins, *Electrochem. Solid-State Lett.*, 2006, **9**, C54.
26 S. N. Chopra, M. F. J. Vos, M. A. Verheijen, J. G. Ekerdt, W. M. M. Kessels and A. J. M. Mackus, *J. Vac. Sci. Technol., A*, 2020, 38.
27 M. Mattinen, J. Hämäläinen, M. Vehkamäki, M. J. Heikkilä, K. Mizohata, P. Jalkanen, J. Räisänen, M. Ritala and M. Leskelä, *J. Phys. Chem. C*, 2016, **120**, 15235.
28 J. Kim, C. Yeon, D. Cho, J. Jung and B. Shong, *Adv. Electron. Mater.*, 2023, 10.
29 O.-K. Kwon, J.-H. Kim, H.-S. Park and S.-W. Kang, *J. Electrochem. Soc.*, 2004, **151**, G109.
30 J. Lu and J. W. Elam, *Chem. Mater.*, 2015, **27**, 4950.
31 N. Leick, S. Agarwal, A. J. M. Mackus and W. M. M. Kessels, *Chem. Mater.*, 2012, **24**, 3696.
32 S. H. Oh, J. M. Hwang, H. Park, D. Park, Y. E. Song, E. C. Ko, T. J. Park, T. Eom and T. Chung, *Adv. Mater. Interfaces*, 2023, 10.
33 S. Dutta, K. Sankaran, K. Moors, G. Pourtois, S. Van Elshocht, J. Bömmels, W. Vandervorst, Z. Tőkei and C. Adelmann, *J. Appl. Phys.*, 2017, 12.
34 N. K. Oh, J.-T. Kim, J.-K. Ahn, G. Kang, S. Y. Kim and J.-Y. Yun, *Appl. Sci. Converg. Technol.*, 2016, **25**, 56.
35 Y. Kotsugi, S.-M. Han, Y.-H. Kim, T. Cheon, D. K. Nandi, R. Ramesh, N.-K. Yu, K. Son, T. Tsugawa, S. Ohtake, R. Harada, Y.-B. Park, B. Shong and S.-H. Kim, *Chem. Mater.*, 2021, **33**, 5639.
36 J. J. Plombon, E. Andideh, V. M. Dubin and J. Maiz, *Appl. Phys. Lett.*, 2006, 89.
37 U. Mizutani and U. Rokakuho, *Introduction to the Electron Theory of Metals*, 2001.
38 E. C. Ko, J. Y. Kim, H. Rhee, K. M. Kim and J. H. Han, *Mater. Sci. Semicond. Process.*, 2022, **156**, 107258.
39 T. Aaltonen, M. Ritala, Y.-L. Tung, Y. Chi, K. Arstila, K. Meinander and M. Leskelä, *J. Mater. Res.*, 2004, **19**, 3353.
40 A. F. Mayadas and M. Shatzkes, *Phys. Rev. B*, 1970, **1**, 1382.
41 T. Aaltonen, P. Alén, M. Ritala and M. Leskelä, *Chem. Vap. Depos.*, 2003, **9**, 45.
42 A. Perron, O. Politano and V. Vignal, *Surf. Interface Anal.*, 2008, **40**, 518.
43 A. Vorobiev, M. Löffler, E. Olsson and S. Gevorgian, *J. Appl. Phys.*, 2014, 115.

Open Access Article. Published on 12 March 2026. Downloaded on 4/4/2026 11:51:12 PM.
This article is licensed under a Creative Commons Attribution 3.0 Unported Licence.

44 Z. Xin, S. Xiao-Hui and Z. Dian-Lin, *Chin. Phys. B*, 2010, **19**, 086802.
45 B.-J. Lee, Y.-S. Kim, D.-W. Seo and J.-W. Choi, *Coatings*, 2023, **13**, 104.
46 A. Marmorstein, A. T. Voutsas and R. Solanki, *J. Appl. Phys.*, 1997, **82**, 4303.
47 O. Kim, Y. Choi, C. Kim, H.-L. Kim and W.-J. Lee, *Ceram. Int.*, 2024, **50**, 45044.
48 Y. Wang, A. Lafosse and K. Jacobi, *Surf. Sci.*, 2002, **507–510**, 773.
49 X. Lu, J. Zhang, W.-K. Chen and A. Roldan, *Nanoscale Adv.*, 2021, **3**, 1624.
50 C. H. Mak, J. L. Brand, A. A. Deckert and S. M. George, *J. Chem. Phys.*, 1986, **85**, 1676.
51 J. A. Herron, S. Tonelli and M. Mavrikakis, *Surf. Sci.*, 2013, **614**, 64.
52 I. N. Yakovkin, *Phys. Chem. Chem. Phys.*, 2009, **11**, 5695.
53 V. P. Zhdanov, J. Pavlíček and Z. Knor, *Catal. Rev.: Sci. Eng.*, 1988, **30**, 501–517.
54 P. M. George, N. R. Avery, W. H. Weinberg and F. N. Tebbe, *Formation and Identification of Methylene on RU(001)*, Division of Chemistry and Chemical Engineering, California Institute of Technology, 1983.
55 Y. Jiao, H. Ma, H. Wang, Y.-W. Li, X.-D. Wen and H. Jiao, *Catal. Sci. Technol.*, 2020, **11**, 191.
56 S. Kumar, C. Multunas, B. Defay, D. Gall and R. Sundararaman, *Phys. Rev. Mater.*, 2022, 6.
57 S. Maîtrejean, R. Gers, T. Mourier, A. Toffoli and G. Passemard, *Microelectron. Eng.*, 2006, **83**, 2396.
58 Y.-Y. Fang, Y.-H. Tsai, Y.-L. Chen, D.-J. Jhan, M.-Y. Lu, P. Y. Keng and S.-Y. Chang, *Appl. Phys. Lett.*, 2024, 124.
59 S. Takamoto, C. Shinagawa, D. Motoki, K. Nakago, W. Li, I. Kurata, T. Watanabe, Y. Yayama, H. Iriguchi, Y. Asano, T. Onodera, T. Ishii, T. Kudo, H. Ono, R. Sawada, R. Ishitani, M. Ong, T. Yamaguchi, T. Kataoka, A. Hayashi, N. Charoenphakdee and T. Ibuka, *Nat. Commun.*, 2022, 13.
60 S. Takamoto, D. Okanohara, Q.-J. Li and J. Li, *J. Materiomics*, 2023, **9**, 447.
61 K. Nakago, torch-dftd, https://github.com/pfnet-research/torch-dftd, accessed: October, 2024.
62 J. Moon, U. Jeon, S. Choung and J. W. Han, *Cell Rep. Phys. Sci.*, 2025, **6**(12), 102968.
63 H. Nakatsubo, D. Mohapatra, E.-S. Lee, J. Kim, I. Cho, M. Iseki, T. Shigetomi, R. Harada, S.-W. Na, T. Cheon, B. Shong and S.-H. Kim, *Adv. Sci.*, 2025, **12**(8), e19209.

This journal is © The Royal Society of Chemistry 2026